Available online at www.sciencedirect.com
SCIENCE DIRECT
International Journal of Heat and Mass Transfer 49 (2006) 1195–1204
International Journal of HEAT and MASS TRANSFER
www.elsevier.com/locate/ijhmt

Lattice Boltzmann method simulation of backward-facing step on convective heat transfer with field synergy principle

Chao-Kuang Chen *, Tzu-Shuang Yen, Yue-Tzu Yang

Department of Mechanical Engineering, National Cheng Kung University, Tainan 70101, Taiwan, ROC

Received 13 June 2005; received in revised form 27 August 2005
Available online 18 October 2005

Abstract

The lattice Boltzmann method (LBM) is applied to simulate the two-dimensional incompressible steady low Reynolds number backward-facing step flows. In order to restrict the approach to the two-dimensional flow, the largest Reynolds number chosen was $Re = 200$. To increase the uniformity of the radial temperature profile for fluid flow in channel and consequently to enhance the heat transfer, the inserted square blockage is used and investigated numerically. In addition, the field synergy principle is also applied to demonstrate that an interruption within fluid results in decreased intersection angle between the velocity and temperature gradient. The numerical results of velocity and temperature field agree well with the available experimental and numerical results.

Keywords: Lattice Boltzmann method; Backward-facing step; Heat transfer; Field synergy principle

1. Introduction

The kinetic nature of the lattice Boltzmann method (LBM) as a relatively new numerical scheme has achieved considerable success in simulating fluid flows and associated transport phenomena in the pass ten years [1]. Unlike conventional numerical schemes based on discretizations of macroscopic continuum equation, the LBM is based on microscopic models and mesoscopic kinetic equation. These algorithms are based on the idea of trying to model a fluid by simulating a discretized one-particle phase space distribution function similar to the one described by the traditional Boltzmann equation. It treats the fluid on a statistical level and simulates the movement and interaction of single particle or ensemble-average particle density distribution function by solving a velocity discrete Boltzmann equation. The fundamental idea of the LBM is to construct simplified kinetic models that incorporate the essential physics of microscopic or mesoscopic processes so that the macroscopic averaged properties obey the desired macroscopic equations.

The lattice Boltzmann equation as a numerical scheme was first proposed by McNamara and Zanetti [2]. It neglects individual particle motion and results in smooth macroscopic behavior. Higuera and co-workers [3,4] introduced a linearized collision operator to simplify the scheme and statistical noise is completely eliminated in both models. A particularly simple linearized version of the collision operator makes use of a relaxation time towards an equilibrium value using a single relaxation time parameter. The relaxation term is known as the Bhatnagar–Gross–Krook (BGK) collision operator [5]. This model is called the lattice Boltzmann BGK model. Use of this collision operator makes the computations much faster. Due to the extreme simplicity, the lattice BGK (LBGK) equation [6] has become the most popular lattice Boltzmann model.

The channel flow over a backward-facing step is often used to evaluate the accuracy of various numerical schemes. The main character is a recirculation region just downstream of the step. At the enlargement, the flow

* Corresponding author. Tel.: +886 6 275 7575x62140; fax: +886 6 234 2081.
E-mail address: ckchen@mail.ncku.edu.tw (C.-K. Chen).

0017-9310/$ - see front matter © 2005 Elsevier Ltd. All rights reserved.
doi:10.1016/j.ijheatmasstransfer.2005.08.027

Nomenclature

c	lattice streaming speed
c_p	specific heat capacity
c_s	sound of speed
ER	channel expansion ratio, H/h
f_α	density distribution function
f_α^{eq}	equilibrium distribution function for f_α
g_α	energy distribution function
g_α^{eq}	equilibrium distribution function for g_α
H	channel width downstream of step
h	step height
Int	integral, $\mathrm{Int} = \int_\Omega \rho c_p(\vec{V}\cdot\nabla T)\,\mathrm{d}x\,\mathrm{d}y$
k	thermal conductivity
Nu	Nusselt number
$\overline{Nu}$	average Nusselt number
Pe	Pelect number, $Pr * Re$
Pr	Prandtl number
p	pressure
Re	Reynolds number
T	temperature
T^*	dimensionless temperature $T - T_w/T_{in} - T_w$
U	maximum velocity in the inlet
$\vec{V}$	velocity vector
w	inserted square blockage width
X_R	reattachment location

Greek symbols

τ_υ	relaxation time for f_α
τ_c	relaxation time for g_α
ε	internal energy
χ	diffusivity
Ω	integral area
ρ	density
υ	kinematic viscosity
δ	small parameter
δx	lattice spacing
δt	time step
θ	intersection angle between the velocity and temperature gradient

Subscripts

in	inlet
m	mean
w	wall

velocity is suddenly reduced and as a consequence the pressure is increased. Fluid particles near the lower wall are unable to negotiate the sudden "drop", causing the formation of a recirculation bubble just downstream of the sudden enlargement. As a result, the prediction of such quantities as the reattachment length (length of the recirculation bubble downstream of the step) tends to compare poorly with experimental data.

The length of the recirculation region is a function of the geometry (expansion ratio), the fluid momentum (Reynolds number) as well as the flow regime (laminar or turbulent). Also there are three important parameters which exert a great influence on the fluid mechanics and heat transfer in the backward-facing step, i.e. Reynolds number Re, channel expansion ER, and Prandtl number Pr. Such a flow pattern has a large number of practical engineering applications, including airfoils, electrical device, diffuser, and combustors. Kondoh et al. [7] used traditional CFD method to simulate laminar heat transfer in a separating and reattaching flow, and the numerical results agree very well with the experiment data of Aung [8] and Hall and Pletcher [9].

Based on an analog between heat convection and heat conduction, Guo and co-workers [10,11] studied the mechanism of convective heat transfer from a second look and proposed novel approaches of enhancing convective heat transfer under the parabolic fluid flow structure. The convection term can be transformed into the form of dot product of velocity and temperature gradient, and integrated the energy equation over the thermal boundary layer. These novel approaches involve improving the uniformity of velocity and temperature profiles as well as reducing the included angle between dimensionless velocity and temperature gradient vectors. Tao and co-workers [12,13] called this concept the field synergy principle and extended from parabolic to elliptic fluid flow and other transport phenomenon. The field synergy theorem was also applied to analyze the thermal performance of our cases.

The objective of this paper is to investigate the velocity and temperature field of this unique recirculation flow and compare the predictions with available experimental and numerical results.

2. Numerical method

2.1. Lattice Boltzmann hydrodynamics model

The nine-velocity LBM model on the 2D square lattice in Fig. 1, denoted as D2Q9 model, is used in the current

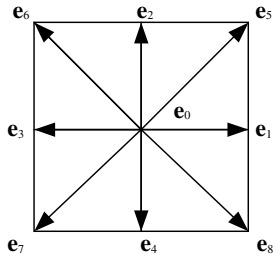

Fig. 1. The nine-velocity LBM model on the 2-D square lattice.

study for simulating the steady backward-facing step. Let $c = \delta x/\delta t = \delta y/\delta t$ be the lattice streaming speed and δx and δy be the distance a particle moves of grid spacing. The discrete velocities for D2Q9 model are defined as follows:

$$\begin{aligned}
&\vec{e}_\alpha = (0,0), \quad \alpha = 0, \text{ rest particle} \\
&\vec{e}_\alpha = (\pm c, 0), (0, \pm c), \quad \alpha = 1,2,3,4 \\
&\vec{e}_\alpha = (\pm c, \pm c), \quad \alpha = 5,6,7,8
\end{aligned} \tag{1}$$

The LBM solves the microscopic kinetic equation for particle distribution $f(\vec{x}, \vec{V}, t)$, where $\vec{x}$ and $\vec{V}$ is the particle position and velocity vector, in phase space $(\vec{x}, \vec{V})$ and time t. The governing equation for density distribution function is

$$f_\alpha(\vec{x} + \vec{e}_\alpha \delta t, t + \delta t) - f_\alpha(\vec{x}, t) = -\frac{1}{\tau_\upsilon}[f_\alpha(\vec{x}, t) - f_\alpha^{\mathrm{eq}}(\vec{x}, t)] \tag{2}$$

where τ_υ characterizes the relaxation time of the density distribution function towards the local equilibrium f_α^{eq}. The equilibrium density distribution is given as

$$f_\alpha^{\mathrm{eq}} = w_\alpha \rho \left[1 + \frac{3\vec{e}_\alpha \cdot \vec{V}}{c^2} + \frac{9}{2}\frac{(\vec{e}_\alpha \cdot \vec{V})^2}{c^4} - \frac{3}{2}\frac{\vec{V}^2}{c^2}\right] \tag{3}$$

where $w_0 = \frac{4}{9}$, $w_\alpha = \frac{1}{9}$ for $\alpha = 1$, 2, 3, 4, $w_\alpha = \frac{1}{36}$ for $\alpha = 5$, 6, 7, 8.

The macroscopic density, velocity are calculated by

$$\rho = \sum_\alpha f_\alpha \tag{4}$$

$$\rho \vec{V} = \sum_\alpha \vec{e}_\alpha f_\alpha \tag{5}$$

Following the same procedure as Hou et al. [14], the continuity and Navier–Stokes equation can be recovered through the Chapman–Enskog expansion for the density distribution function. The detail of derivation of this is given by Hou and will not be shown here. If only the physics in the long-wave-length and low-frequency limit are of interest, the lattice spacing δx and the time increment δt can be regarded as small parameters of the same order δ. The final results of the Navier–Stokes equation and continuity equation are as below:

$$\partial_t \rho + \nabla \cdot (\rho \vec{V}) = 0 + \mathrm{O}(\delta^2) \tag{6}$$

$$\partial_t (\rho \vec{V}) + \nabla \cdot (\rho \vec{V}\vec{V}) = -\nabla p + \upsilon[\nabla^2(\rho \vec{V}) + \nabla(\nabla \cdot (\rho \vec{V}))] + \mathrm{O}(\delta^2) \tag{7}$$

where $p = c_s^2 \rho$ is the pressure from the equation of state for the ideal gas, $c_s = c/\sqrt{3}$ is the sound speed, and the kinematic viscosity is given by

$$\upsilon = \frac{(2\tau_\upsilon - 1)}{6}\frac{(\delta x)^2}{\delta t} \tag{8}$$

The Mach number is $M = \vec{V}/c_s$ and a low Mach number assumption invoked as the nearly incompressible limit is approached, i.e., $M \ll 1$. The incompressible Navier–Stokes equation and continuity equation are expressed as

$$\nabla \cdot \vec{V} = 0 + \mathrm{O}(\delta^2) \tag{9}$$

$$\partial_t \vec{V} + \vec{V} \cdot \nabla \vec{V} = -\frac{\nabla p}{\rho} + \upsilon \nabla^2 \vec{V} + \mathrm{O}(\delta^2) \tag{10}$$

2.2. Lattice Boltzmann thermal model

Generally speaking, the current thermal models fall into the following classifications: the multispeed approach [15], the passive scalar temperature distribution approach [16] and the thermal energy distribution model proposed by He et al. [17]. The multispeed approach suffers severe numerical instability, and the temperature variation is limited to a narrow range and fixed Prandtl number. The passive scalar temperature distribution approach neglects viscous heat dissipation and compression work done by pressure. The thermal energy distribution model is an adequate tool for solving real thermal problems. But there still exist some shortcomings for this thermal model. First, it contains one complicated gradient operator term in the evolution equation for the temperature, and the simplicity property of the LBM has been lost. Second, since the viscosity is involved not only in the momentum equation but also in the energy equation, the new variables for the thermal energy distribution function are used in order to keep the viscosity consistent in the governing equations for the thermal energy distribution model and to avoid the implicitness of the schemes [17]. So, we decided to choose the simplified thermal model which is proposed by Peng et al. [18]. The simplified thermal model consider the fact that the compression work done by the pressure and the viscous heat dissipation can be neglected for the incompressible flow, so the gradient term can be dropped out in the evolution equation since such gradient term is mainly used to recover these term through the Chapman–Enskog expansion.

The governing equation for simplified thermal energy distribution model is

$$g_\alpha(\vec{x} + \vec{e}_\alpha \delta t, t + \delta t) - g_\alpha(\vec{x}, t) = -\frac{1}{\tau_c}[g_\alpha(\vec{x}, t) - g_\alpha^{\mathrm{eq}}(\vec{x}, t)] \tag{11}$$

Following the work of He et al. [17], the equilibrium energy distribution functions g can be written as

$$g_0^{\mathrm{eq}} = -\frac{2\rho\varepsilon}{3}\frac{\vec{V}^2}{c^2} \tag{12}$$

$$g_{1,2,3,4}^{\mathrm{eq}} = \frac{\rho\varepsilon}{9}\left[\frac{3}{2} + \frac{3}{2}\frac{\vec{e}_\alpha \cdot \vec{V}}{c^2} + \frac{9}{2}\frac{(\vec{e}_\alpha \cdot \vec{V})^2}{c^4} - \frac{3}{2}\frac{\vec{V}^2}{c^2}\right] \tag{13}$$

$$g_{5,6,7,8}^{\mathrm{eq}} = \frac{\rho\varepsilon}{36}\left[3 + 6\frac{\vec{e}_\alpha \cdot \vec{V}}{c^2} + \frac{9}{2}\frac{(\vec{e}_\alpha \cdot \vec{V})^2}{c^4} - \frac{3}{2}\frac{\vec{V}^2}{c^2}\right] \tag{14}$$

where $\varepsilon = DRT/2$. In this equation R is the gas constant and D is the dimension. Then the macroscopic temperature are calculated by

$$\rho\varepsilon = \sum_{\alpha} g_{\alpha} \tag{15}$$

Following the same procedure as presented by Hou et al. [14], the Chapman–Enskog expansion for the new thermal energy distribution function can recover macroscopic energy equation. Using $g_{\alpha}^{(0)}$ instead of g_{α}^{eq} and expanding g_{α} about $g_{\alpha}^{(0)}$, it can be described by the following equation:

$$g_{\alpha} = g_{\alpha}^{(0)} + \delta g_{\alpha}^{(1)} + \delta^2 g_{\alpha}^{(2)} + \mathrm{O}(\delta^3) \tag{16}$$

where δ is the expansion parameter. To discuss changes in different time scale, t_0 and t_1 are introduced as $t_0 = t$, $t_1 = \delta t, \ldots$; thus

$$\partial_t = \partial_{t0} + \delta\partial_{t1} + \delta^2\partial_{t2} + \cdots \tag{17}$$

The first-order expansion of Eq. (11) is

$$(\partial_{t0} + \vec{e}\cdot\nabla) g_{\alpha}^{(0)} = -\frac{1}{\tau_{\mathrm{c}}} g_{\alpha}^{(1)} \tag{18}$$

The second-order expansion of Eq. (11) is

$$\partial_{t1} g_{\alpha}^{(0)} + \left(1 - \frac{1}{2\tau_{\mathrm{c}}}\right)(\partial_{t0} + \vec{e}\cdot\nabla) g_{\alpha}^{(1)} = -\frac{1}{\tau_{\mathrm{c}}} g_{\alpha}^{(2)} \tag{19}$$

Taking summation of Eqs. (18) and (19), we can get

$$\partial_{t0}(\rho\varepsilon) + \nabla\cdot(\rho\vec{V}\varepsilon) = 0 \tag{20}$$

$$\partial_{t1}(\rho\varepsilon) + \left(1 - \frac{1}{2\tau_{\mathrm{c}}}\right)\Pi^{(1)} = 0 \tag{21}$$

where $\Pi^{(1)} = -\frac{2}{3}\tau_{\mathrm{c}}\nabla^2(\rho\varepsilon)$. Combining Eqs. (20) and (21), we can get

$$\partial_t(\rho\varepsilon) + \nabla\cdot(\rho\vec{V}\varepsilon) = \chi\nabla^2(\rho\varepsilon) + \mathrm{O}(M^2\delta T) \tag{22}$$

and the diffusivity χ is determined by

$$\chi = \frac{2}{3}\left(\tau_{\mathrm{c}} - \frac{1}{2}\right)\delta t \tag{23}$$

No matter in Eq. (2) or (11) we choose, it should be solved in collision and streaming two steps. The streaming step needs little computational effort by advancing the data from neighbor lattice points and the collision step is completely localized.

2.3. Implementation of the boundary conditions

The implementation of the boundary condition is very important in the simulation. A difficulty of the LBM is that the boundary conditions for the distribution function are not known. One must construct suitable conditions for f_{α} and g_{α} based on the macroscopic flow variables. This study concerns three cases with different thermal boundary condition as below:

Case A: The thermal boundary condition is the same as Kondoh et al. [7] and at the step-side lower wall downstream of the step is kept constant high temperature, which is assumed to be higher than inlet temperature. The other part of the wall is treated as adiabatic.

Case B: The constant higher inlet temperature and the other part of the walls are assumed constant lower temperature.

Case C: Add an inserted square blockage in the backward-facing step geometry. The thermal boundary condition is the same as case B. To eliminate the effect of other factors, the inserted blockage is particularly assumed to be thermally isolated from other heat source. The only function is to introduce interruption within the fluid.

The non-uniform grid is used for all of the following numerical simulations. In each run, the following inequality is used as the criterion of convergence,

$$\frac{\sum_{i,j}\|\vec{V}(x_{i,j}, t+\delta t) - \vec{V}(x_{i,j}, t)\|}{\sum_{i,j}\|\vec{V}(x_{i,j}, t)\|} \leqslant 1.0\times 10^{-6} \tag{24}$$

$$\frac{\sum_{i,j}\|T(x_{i,j}, t+\delta t) - T(x_{i,j}, t)\|}{\sum_{i,j}\|T(x_{i,j}, t)\|} \leqslant 1.0\times 10^{-6} \tag{25}$$

where $\|*\|$ is the L_2 norm.

2.3.1. The boundary condition of the velocity field

At inlet the uniform velocity flow is applied and the velocity is fixed at 0.05. The velocity was chosen to be lower than 10% of the speed of sound for the LBM simulation to avoid significant compressibility effects which are known to increase with the square of the Mach number. Using the bounce-back rule of the non-equilibrium distribution proposed by Zou and He [19] and the equilibrium density distribution function was computed from the pressure and the given velocity and imposed at the first lattice column. At the outlet a fixed pressure is imposed in terms of the equilibrium distribution function. The velocity components are extrapolated upstream.

The bounce-back rule of the non-equilibrium distribution proposed by Zou and He [19] is also used here for no slip boundary condition on the wall. The density distribution function at the boundary need to satisfy the following condition:

$$f_{\alpha}^{\mathrm{neq}} = f_{\beta}^{\mathrm{neq}} \tag{26}$$

where e_{α} and e_{β} have opposite directions. The velocity of the wall is used when f^{eq} for the boundary nodes are calculated in order to enforce the no-slip boundary condition.

2.3.2. The boundary condition of the temperature field

For the thermal problem, the thermal energy distribution function at the boundary satisfied:

$$g_{\alpha}^{\mathrm{neq}} - e_{\alpha}^2 f_{\alpha}^{\mathrm{neq}} = -(g_{\beta}^{\mathrm{neq}} - e_{\beta}^2 f_{\beta}^{\mathrm{neq}}) \tag{27}$$

The temperature of the wall is also used when g^{eq} for the boundary nodes are calculated in order to satisfy the given temperature. Neumann and Dirichlet boundary conditions are used in the study. For the Dirichlet type condition, the given temperature is applied on the boundary. For the Neumann type condition (adiabatic or constant heat flux), it was transferred to the Dirichlet type condition through

the conventional second-order finite difference approximation to get the temperature on the boundary [20]. When the temperature gradient is given, the temperature on the boundary can be calculated by

$$\left.\frac{\partial T}{\partial y}\right|_{x,1} = \frac{-3T_{x,1} + 4T_{x,2} - T_{x,3}}{2\Delta y} \tag{28}$$

No matter the adiabatic or constant heat flux boundary condition we choose, through the Eq. (28) we can get the corresponding Dirichlet type boundary condition.

2.4. Taylor series expansion and least square based LBM (TLLBM)

The method proposed by Shu et al. [21] is based on the well-known fact that the density and energy distribution functions are continuous function in physical space and can be well defined in any mesh system. It is derived from the standard LBM by using Taylor series expansion and optimized by the least squares method. This method explicitly updates the distribution functions at mesh points by an algebraic formulation and the relevant coefficients are precomputed from the coordinates of mesh points. As shown in Fig. 2, point A represent the position (x_A, y_A), point A' represent the position $(x_A + e_{\alpha x}\delta t, y_A + e_{\alpha y}\delta t)$, and point P represent the position (x_P, y_P). The distribution functions of the points A', B', C', D', E', P' can be got from Eqs. (2) and (11). For the general case, A' may not coincide with the mesh point P. So Taylor series expansion in the spatial direction is applied in this method. $f_\alpha(A', t+\delta t)$ can be approximated by the corresponding function and its derivatives at mesh point P as

$$\begin{aligned} f_\alpha(A', t+\delta t) &= f_\alpha(P, t+\delta t) + \Delta x_A \frac{\partial f_\alpha(P, t+\delta t)}{\partial x} + \Delta y_A \frac{\partial f_\alpha(P, t+\delta t)}{\partial y} \\ &+ \frac{1}{2}(\Delta x_A)^2 \frac{\partial^2 f_\alpha(P, t+\delta t)}{\partial x^2} + \frac{1}{2}(\Delta y_A)^2 \frac{\partial^2 f_\alpha(P, t+\delta t)}{\partial y^2} \\ &+ \Delta x_A \Delta y_A \frac{\partial^2 f_\alpha(P, t+\delta t)}{\partial x \partial y} + O[(\Delta x_A)^3, (\Delta y_A)^3] \end{aligned} \tag{29}$$

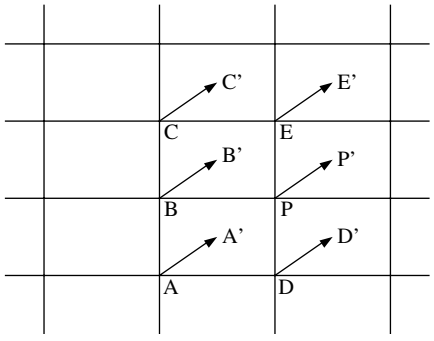

Fig. 2. Configuration of particle movement along α direction.

It means that after collision there is no information streaming to the point P and we can use point A' to obtain the information of point P. It also needs neighboring five points around P because the RHS of Eq. (29) exist six unknown. The unknown can be decided from the least square method.

3. Results and discussion

3.1. Overview of the velocity field

The simulation of the flow with a nonuniform rectangular mesh (601 * 61) in Fig. 3 was conducted. Uniform square lattice mesh was used before the recirculation zone and nonuniform rectangular mesh was used after the recirculation zone. The ratio of nonuniform to uniform grid size in x direction is 2. Due to the computational mesh is uncoupled from the discretization of momentum space and it can have an arbitrary space. Channel expansion ratio, ER, is defined as H/h. The Reynolds number Re of the flow is defined as $4U(H-h)/3\upsilon$, where U is the maximum velocity in the inlet. The velocity vector plots of Fig. 4 provides an overall view of the flow under conditions where ER = 2 and $Re = 105$. As might be expected, there was a recirculation zone behind the step. The locations of the reattachment points for $Re = 100$ and 200 are $X_R/h =$ 3.18 and 5.5 respectively. This discrepancy of the reattachment locations with the experimental data of Armaly et al. [22], $X_R/h = 3.1$ and 5.4 for $Re = 100$ and 200 respectively, can be attributed to the slight difference in the geometric configuration of the flow. But the numerical data is close to the result of He [23], where $X_R/h = 3.15$ with $Re =$ 100. As expected, a larger Reynolds number increases the length of flow redevelopment downstream of the step.

Fig. 5 shows the velocity vector field with the inserted square blockage after the enlargement. The flow field

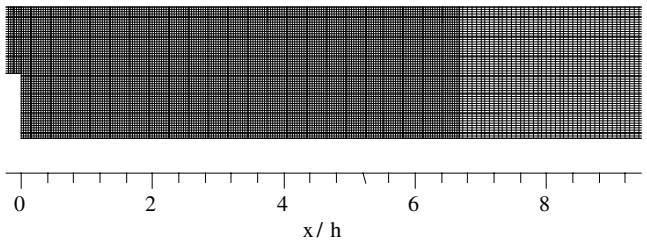

Fig. 3. Non-uniform mesh for the backward-facing step flow simulation.

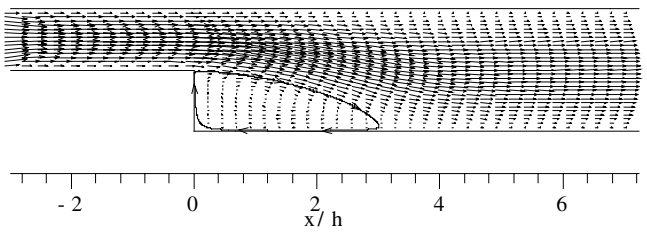

Fig. 4. Velocity field without blockage (ER = 2, $Re = 105$).

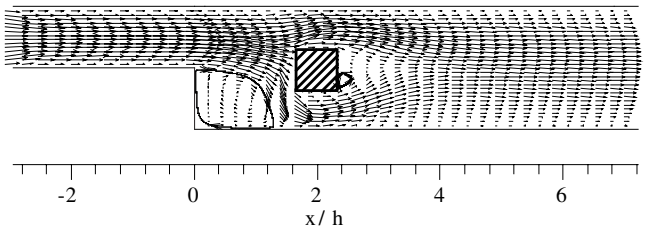

Fig. 5. Velocity field with square blockage (ER = 2, $Re = 105$).

characteristic is different from Fig. 4 and the recirculation region is narrowed due to the interruption within flow. There is also a small recirculation zone behind the blockage and the overall flow structure is reasonably well predicted.

3.2. Influence of Reynolds number and channel expansion ratio

The boundary condition of case A is the same as Kondoh et al. [7] and is convenient for comparison. The result is presented in Fig. 6, and it shows the influence of the Reynolds number Re on the local heat transfer distribution on the bottom heat transfer surface with ER = 1.5 and $Pr = 0.7$. As the Reynolds number increases, the peak value of Nu moves downstream accompanied by a consistently growing peak value. This movement of the peak values of Nu seems to be related to the movement of the flow attachment length. It revealed that the numerical data agrees well with the results of Kondoh et al. [7] except near the step. The variation of the local heat transfer characteristics with Reynolds number can be interpreted by the temperature distributions presented in Fig. 7. As shown in the figure, the temperature contours for the non-dimensional temperature T^* in increments of 0.1 are displayed. Under the influence of the reattachment flow, the temperature contours undergo local distortion around the flow reattachment point. The thermal boundary layer is then compressed by the reattachment wall-ward flow. Consequently a layer with a steep temperature gradient is formed above the wall around the flow reattachment point. This leads to the heat transfer enhancement there. Because the recirculation flow continues to convey there the high temperature fluid

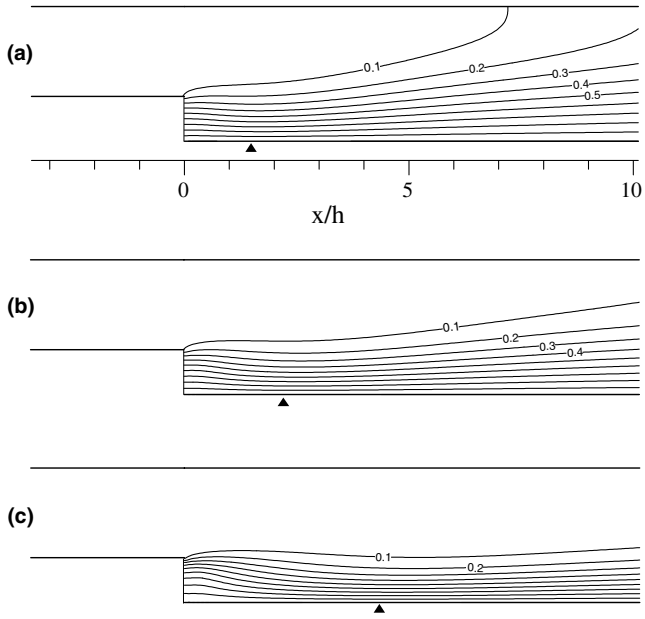

Fig. 7. The temperature distribution for case A (a) $Re = 10$, (b) $Re = 20$ and (c) $Re = 50$ (ER = 1.5, $Pr = 0.7$); (▲) reattachment point.

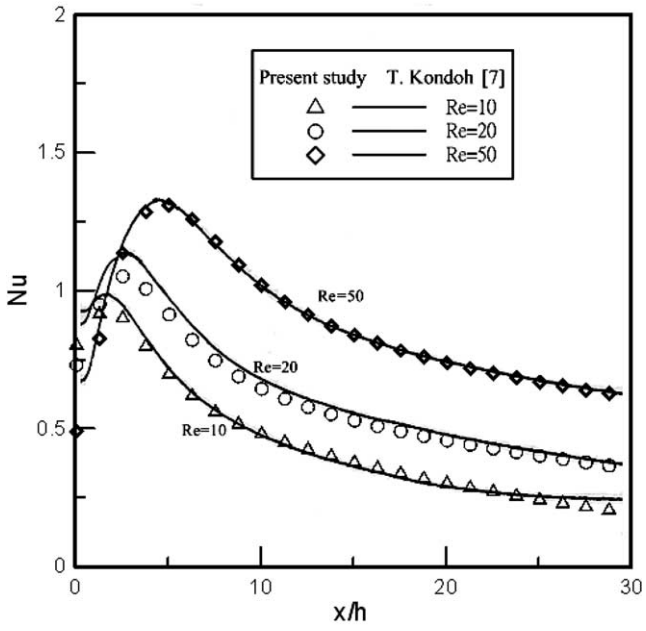

Fig. 6. Comparison of the Nusselt number between Kondoh et al. [7] and the present computation for case A (ER = 1.5, $Pr = 0.7$).

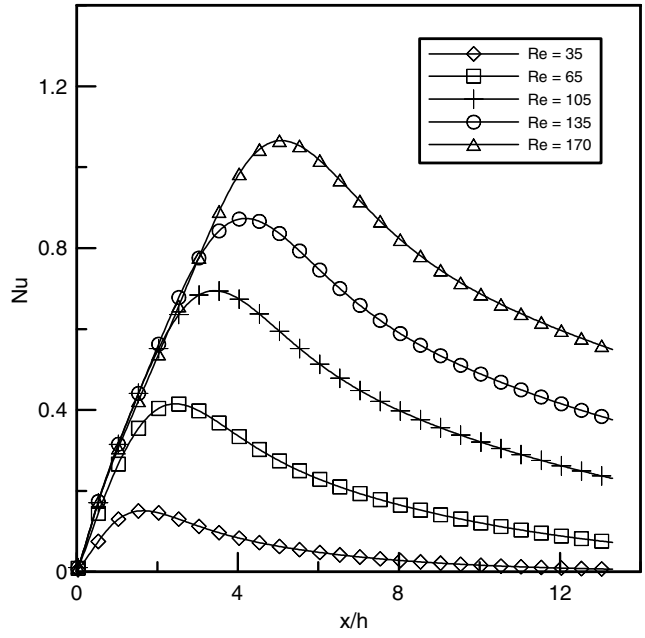

Fig. 8. Effect of Reynolds number on Nusselt number for case B (ER = 2, $Pr = 0.7$).

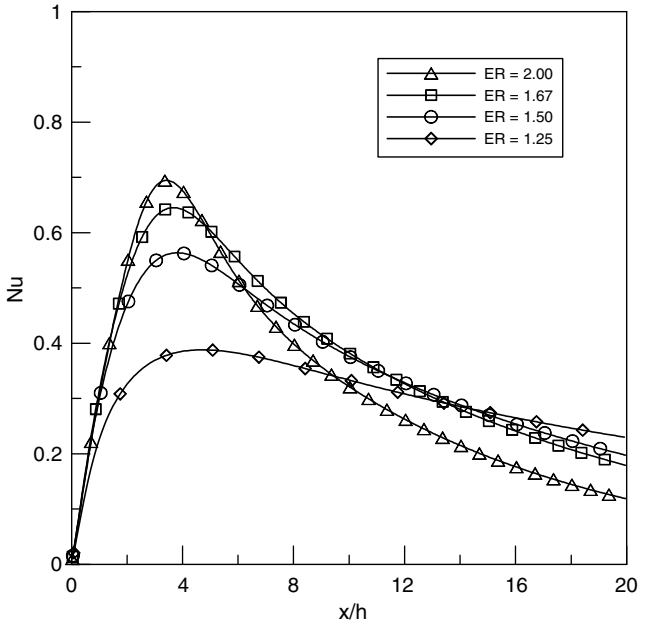

Fig. 9. Effect of channel expansion ratio (ER) on Nusselt number for case B ($Re = 105$, $Pr = 0.7$).

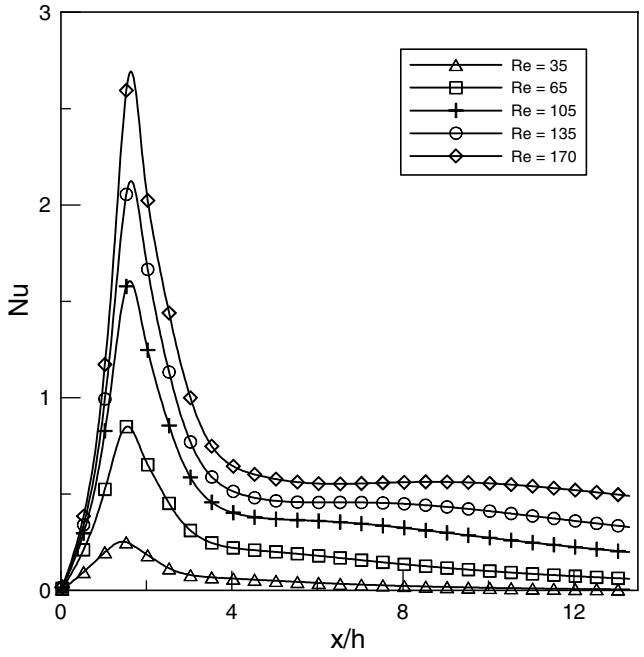

Fig. 10. Effect of Reynolds number on Nusselt number for case C (ER = 2, $Pr = 0.7$).

generated on the heat transfer surface, the temperature variation is concentrated in the separating shear layer just behind the enlargement step.

Fig. 8 shows the influence of the Reynolds number, *Re*, on the local heat transfer distribution on heat transfer surface under case B. It displays almost the same trend as Fig. 6. The different performance is near the step because of the different thermal boundary conditions. Due to the different thermal boundary conditions and Reynolds number definition, the corresponding *Nu* is also different. But the movement of the peak values of *Nu* is still related to the movement of the flow attachment length.

Fig. 9 shows the influence of the channel expansion ratio, ER, on the local heat transfer distribution. The Reynolds number, *Re*, and the Prandtl number, *Pr*, are fixed at 105 and 0.7, respectively. As ER increases, the peak location of *Nu* moves upstream and the peak value grows consistently. This movement of the peak location of *Nu* is considered again to be due to the movement of the flow-attachment point. It is naturally understood that the compression of thermal boundary layer by the reattaching flow becomes stronger with increasing ER.

Case C with a square blockage in the computation domain is demonstrated in Fig. 10 and it shows the influence of the Reynolds number, *Re*, on the local heat transfer distribution. The local *Nu* value is greater than the case without the inserted blockage and the convective heat transfer performance is better than the previous cases.

3.3. Influence of Prandtl number

The influence of the Prandtl number on the temperature distribution and the fundamental heat transfer characteristics was investigated. In the LBM algorithm the *Pr* is defined as

$$Pr = \frac{\upsilon}{\chi} = \frac{\tau_\upsilon - 1/2}{2(\tau_c - 1/2)} \tag{30}$$

When we fixed the *Re*, the τ_υ value was also fixed. The only method to change *Pr* number is to select a different τ_c value. But the relaxation time of energy distribution function has some limitations, and it is difficult to simulate Prandtl number at extreme high and low values. So we choose at $Pr = 1$, 0.7 and 0.4 to simulate. Fig. 11 shows the temperature distribution for various Prandtl numbers in case B with $Re = 105$. The contours in these figures correspond to the non-dimensional temperature T^* in

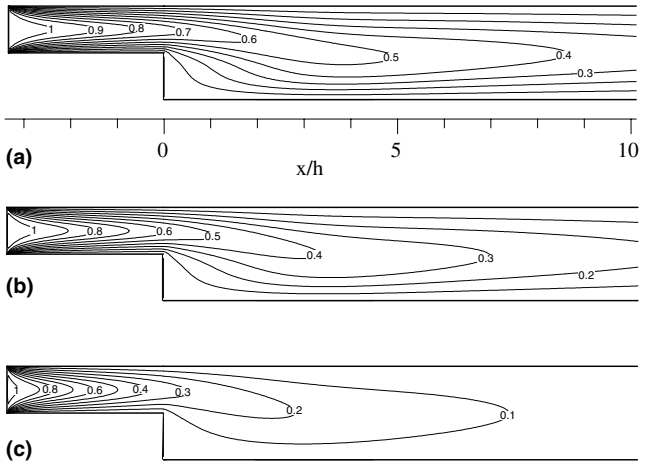

Fig. 11. Effect of Prandtl number on the temperature distribution for case B (a) $Pr = 1.0$, (b) $Pr = 0.7$ and (c) $Pr = 0.4$ (ER = 2, $Re = 105$).

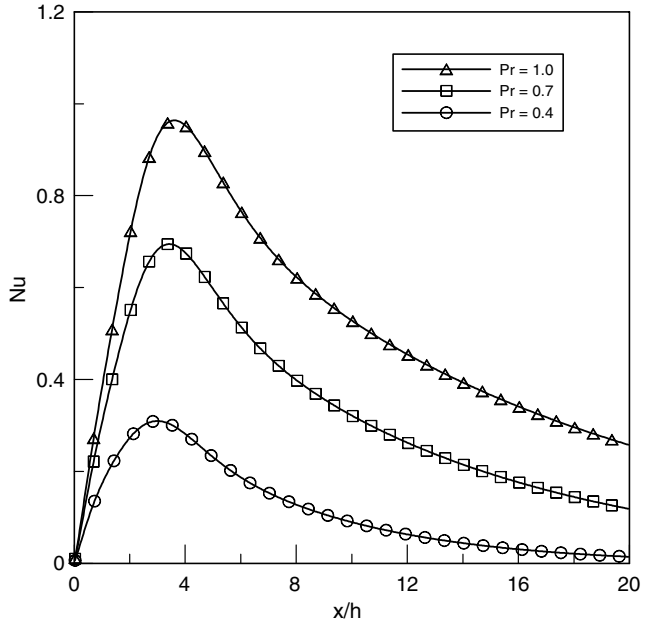

Fig. 12. Effect of Prandtl number on Nusselt number for case B ($Re = 100$, ER = 2).

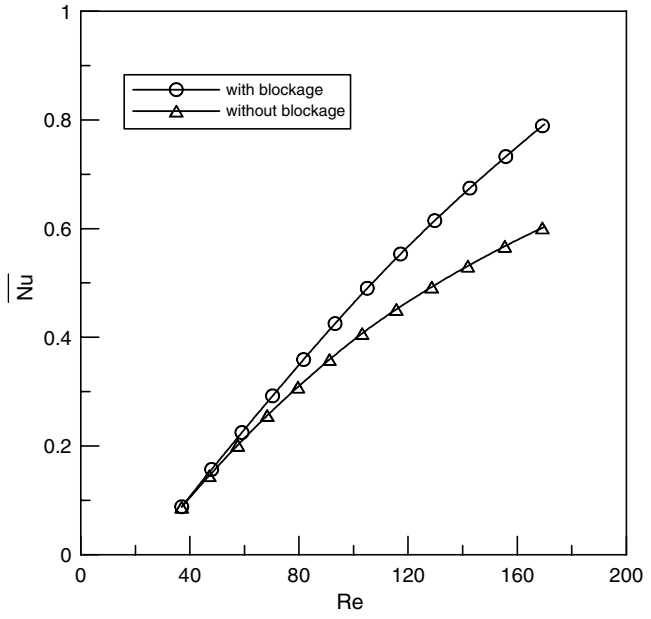

Fig. 14. Effect of Reynolds number on average Nusselt number with or without inserted square blockage.

increments of 0.1. When Prandtl number ranges from 0.4 to 1 (or $Pe = 42$–105), the convection effect dominates in most of the region except in the recirculation region. Additionally, in Fig. 11(a) the convection effect is more evident than in Fig. 11(c).

Fig. 12 shows the local heat transfer distribution on the heat transfer surface for various Prandtl number. The substantial heat transfer enhancement by the reattaching flow is recognized around the flow attachment point. *Nu* Continues to increase with the Prandtl number in the whole region and the heat transfer enhancement around the flow reattachment point becomes more and more evident.

3.4. Numerical demonstrations for the relation between field synergy for enhancing convective heat transfer

The geometric parameter of the inserted square blockage is $w = \frac{1}{3}H$ and the location is as plotted in Fig. 13. From this series of numerical simulations, better heat transfer performance is generated when the location of the inserted blockage is $w = \frac{5}{6}H$ from the step and $\frac{1}{3}H$ from the wall. Fig. 14 reveals the inserted blockage can enhance thermal performance and the effect is more evident when the Reynolds number is high. Insertion of a square blockage increases *Nu* about 33% at $Re = 170$.

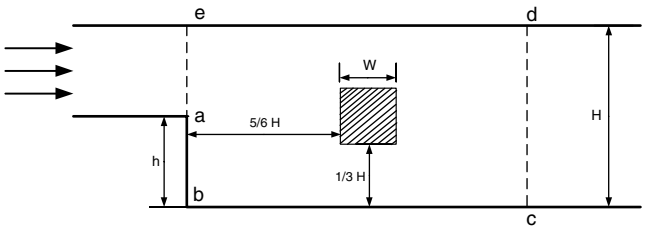

Fig. 13. The geometry of backward-facing step with inserted square blockage.

There are three mechanisms to enhance single phase convective heat transfer. They are: increasing the flow interruption, decreasing the thermal boundary layer, and increasing the velocity gradient near a solid wall [10]. In this section, case C revealed the inherent relation between the field synergy principle and demonstrated that increasing the flow interruption can enhance single phase convective heat transfer.

From the field synergy principle's point of view, there are two parameters except Nusselt number, the Int value and average intersection angle θ_m, can examine the temperature field thermal efficiency.

The steady state 2D incompressible energy equation of fluid flow and heat transfer over a backward facing step is

$$\rho c_p\left(u\frac{\partial T}{\partial x}+v\frac{\partial T}{\partial y}\right)=\frac{\partial}{\partial x}\left(k\frac{\partial T}{\partial x}\right)+\frac{\partial}{\partial y}\left(k\frac{\partial T}{\partial y}\right) \tag{31}$$

The definition of the Int value is defined in Eq. (32) and it actually represents the energy transferred by convection. It implies that the convective heat transfer can be enhanced by raising the value of the integral of the convection term (heat source) over the computation domain.

$$\mathrm{Int}=\int_{\Omega}\rho c_p(\vec{V}\cdot\nabla T)\,\mathrm{d}x\,\mathrm{d}y \tag{32}$$

Tao et al. [13] applied the Gauss theorem for reduction of the integral dimension on the RHS of Eq. (31). Setting Eq. (31) equal to Eq. (32), we obtain

$$\iint_{\Omega=abcdea} \rho c_p(\vec{V}\cdot\nabla T)\,\mathrm{d}x\,\mathrm{d}y = \int_{abc} \vec{n}\cdot k\nabla T\,\mathrm{d}S + \int_{cd} \vec{n}\cdot k\nabla T\,\mathrm{d}S + \int_{de} \vec{n}\cdot k\nabla T\,\mathrm{d}S + \int_{ea} \vec{n}\cdot k\nabla T\,\mathrm{d}S \quad (33)$$

where $\vec{n}$ represents the outward normal vector along each boundary and $\mathrm{d}S$ is the length differential of each boundary. Using Eq. (33) the Int value over the computation domain can be easily calculated. Fig. 15 shows the influence of the Reynolds number, *Re*, on the non-dimensional Int value for a backward-facing step with or without an inserted square blockage. The bigger Int value means that the integral of the convection term and the ability to enhance heat transfer is greater. It also means better synergy. The trend of Fig. 15 is the same as Fig. 14 revealing that the Int value grows larger as *Re* increases and the value with blockage is greater than that without blockage. The effect becomes more and more evident under high *Re*.

Eq. (34) gives us a more insight on convective heat transfer. There are three ways to enhance heat transfer. They are: increasing Reynolds and Prandtl numbers, increasing the fullness of dimensionless velocity and temperature profiles, and increasing the included angle between dimensionless velocity and temperature gradient vectors.

$$RePr\int(\vec{V}\cdot\nabla\vec{T})\,\mathrm{d}y = Nu \quad (34)$$

$$\vec{V}\cdot\nabla T = |\vec{V}||\nabla T|\cos\theta \quad (35)$$

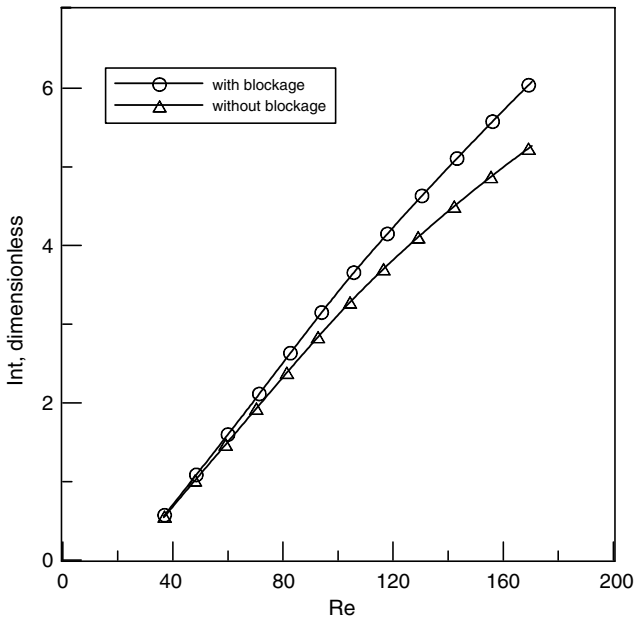

Fig. 15. Effect of Reynolds number on dimensionless Int number with or without inserted square blockage.

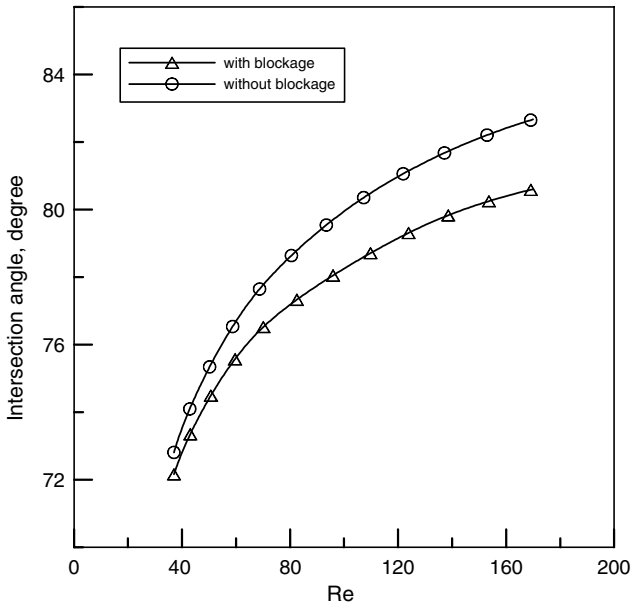

Fig. 16. Effect of Reynolds number on average intersection angle with or without inserted square blockage.

Here, θ_m is the average intersection angle between the velocity vector and the temperature gradient in the computation domain. If the local value of θ is greater than 90°, its value is taken as $(180^\circ - \theta)$ when added to the summation of the intersection angle [12]. Fig. 16 shows the variation of average intersection angles with *Re* for a backward-facing step with or without an inserted square blockage. It is clear that a better synergy means decreasing the intersection angle between the velocity vector and the temperature gradient. This demonstrates that the increased interruption within flow is due to the decreased intersection angle between the velocity and temperature gradient. It decreases about 3° but average Nusselt number increases 33% at $Re = 170$. For the synergy principle, there is still much room to improve the thermal performance in a backward-facing step.

4. Conclusions

In this study, low Reynolds number backward-facing step flows are simulated using single-relaxation-time model in the parallel lattice LBM. The numerical results of velocity and temperature field agree well with the available experimental and numerical results. When we applied field synergy principle on temperature field, we demonstrated that the thermal efficiency can be examined by Nusselt number, Int value, and average intersection angle θ_m. The simplified thermal model which was applied is the proper LBM thermal model and it can simulate incompressible thermal fluid flow properly. Using inserted square blockage can enhance convective heat transfer by way of flow interruption and thermal boundary layer compression.

References

[1] S. Chen, G.D. Doolen, Lattice Boltzmann method for fluid flows, Annu. Rev. Fluid Mech. 30 (1998) 329–364.

[2] G. McNamara, G. Zanetti, Use of the Boltzmann equation to simulate Lattice-Gas Automata, Phys. Rev. Lett. 61 (1988) 2332–2335.

[3] F. Higuera, J. Jimenez, Boltzmann approach to lattice gas simulations, Europhys. Lett. 9 (1989) 663–668.

[4] F. Higuera, S. Succi, R. Benzi, Lattices gas dynamics with enhanced collisions, Europhys. Lett. 9 (1989) 345–349.

[5] P.L. Bhatnagar, E.P. Gross, M. Krook, A model for collision process in gases. I. Small amplitude processes in charged and neutral one-component system, Phys. Rev. 94 (1954) 511–521.

[6] H. Chen, S. Chen, W.H. Matthaeus, Recovery of the Navier–Stokes equation using a lattice Boltzmann method, Phys. Rev. A 45 (1992) 5339–5342.

[7] T. Kondoh, Y. Nagano, T. Tsuji, Computational study of laminar heat transfer downstream of a backward-facing step, Int. J. Heat Mass Transfer 36 (1993) 577–591.

[8] W. Aung, An experimental study of laminar heat transfer downstream of backstep, J. Heat Transfer 105 (1983) 823–829.

[9] E.J. Hall, R.H. Pletcher, An application of a viscous–inviscid interaction procedure to predict separated flows with heat transfer, J. Heat Transfer 107 (1985) 557–563.

[10] Z.Y. Guo, D.Y. Li, B.X. Wang, A novel concept for convective heat transfer enhancement, Int. J. Heat Mass Transfer 41 (1998) 2221–2225.

[11] S. Wang, Z.X. Li, Z.Y. Guo, Novel concept and device of heat transfer augmentation, in: Proc. of 11th IHTC, vol. 5, 1998, pp. 405–408.

[12] W.Q. Tao, Y.L. He, Q.W. Wang, Z.G. Qu, F.Q. Song, A unified analysis on enhancing single phase convective heat transfer with field synergy principle, Int. J. Heat Mass Transfer 45 (2002) 4871–4879.

[13] W.Q. Tao, Z.Y. Guo, B.X. Wang, Field synergy principle for enhancing convective heat transfer—its extension and numerical verifications, Int. J. Heat Mass Transfer 45 (2002) 3849–3856.

[14] S. Hou, Q. Zou, S. Chen, G. Doolen, A.C. Cogley, Simulation of cavity flow by the lattice Boltzmann method, J. Comput. Phys. 118 (1995) 329–347.

[15] F.J. Alexander, S. Chen, J.D. Sterling, Lattice Boltzmann thermohydrodynamics, Phys. Rev. E 47 (1993) R2249.

[16] X. Shan, Solution of Rayleigh–Benard convection using a lattice Boltzmann method, Phys. Rev. E 55 (1997) 2780–2788.

[17] X. He, S. Chen, G.D. Doolen, A novel thermal model for the lattice Boltzmann method in incompressible limit, J. Comput. Phys. 146 (1998) 282–300.

[18] Y. Peng, C. Shu, Y.T. Chew, Simplified thermal lattice Boltzmann model for incompressible thermal flows, Phys. Rev. E. 68 (2003) 026701.

[19] Q. Zou, X. He, On pressure and velocity boundary conditions for the lattice Boltzmann BGK model, Phys. Fluids 9 (1997) 1591–1598.

[20] C. Shu, Y. Peng, Y.T. Chew, Simulation of Natural Convection in a Square Cavity by Taylor series expansion and Least square-based Lattice Boltzmann Method, Int. J. Modern Phys. C 13 (2002) 1399–1414.

[21] C. Shu, X.D. Niu, Y.T. Chew, Taylor-series expansion and least squares-based lattice Boltzmann method: two-dimensional formulation and its application, Phys. Rev. E 65 (2002) 036708.

[22] B.F. Armaly, F. Durst, J.C.F. Pereira, B. Schonung, Experimental and theoretical investigation of backward-facing step flow, J. Fluid Mech. 127 (1983) 473–496.

[23] Xiaoyi He, Li-Shi Luo, A prior derivation of the lattice Boltzmann equation, Phys. Rev. E 55 (1997) 6333–6336.